

# Recent Progress in Terahertz Quantum-Well Photodetectors

X. G. Guo, J. C. Cao, R. Zhang, Z. Y. Tan, and H. C. Liu, *Fellow, IEEE*

(Invited Paper)

**Abstract**—Terahertz quantum-well photodetectors (QWPs) represent a new and emerging photon-type detector in a terahertz region. Recent progress in the development of terahertz QWPs is reviewed. We first discuss the many-particle effects on the accurate design of terahertz QWPs. Second, three types of light couplers for terahertz QWPs are introduced. At resonant coupling frequencies, the polarization of light field is effectively changed by the light couplers to fulfill the selection rule of intersubband transition. Meanwhile, the electric field intensities in the active multiquantum-well region of terahertz QWPs are enhanced. The performance of terahertz QWPs with these light couplers is improved significantly. Finally, terahertz-QWP-based wireless communication and imaging are demonstrated.

**Index Terms**—Imaging, light couplers, quantum-well photodetectors (QWPs), terahertz, wireless communication.

## I. INTRODUCTION

TERAHERTZ detectors are key components in a wide range of applications such as material identification, imaging, tomography, communication, etc. [1]. Various terahertz detectors have been applied in these applications. The thermal terahertz detectors such as Golay cell [2], room-temperature and cooled bolometers [3], [4], and pyroelectric detectors [5] are used in terahertz and far-infrared imaging and spectroscopy with a long history. Semiconductor photoconductive antennas play an important role in terahertz time-domain spectroscopy systems [6].

Manuscript received April 14, 2012; revised May 17, 2012; accepted May 17, 2012. Date of publication May 24, 2012; date of current version February 1, 2013. This work was supported in part by the 863 Program of China (Project 2011AA010205), in part by the National Natural Science Foundation of China (Grants 61176086, 61131006, and 60721004), in part by the Major National Development Project of Scientific Instrument and Equipment (Grant 2011YQ150021), in part by the Important National Science and Technology Specific Projects (Grant 2011ZX02707), in part by the major project (Project YYYJ-1123-1), in part by the Hundred Talent Program of the Chinese Academy of Sciences, and in part by the Shanghai Municipal Commission of Science and Technology (Projects 10JC1417000 and 11ZR1444200). The work of H. C. Liu was supported in part by the National Major Basic Research Project (2011CB925603) and in part by the Shanghai Municipal Major Basic Research Project (09DJ1400102).

X. G. Guo, J. C. Cao, R. Zhang, and Z. Y. Tan are with the Key Laboratory of Terahertz Solid-State Technology, Shanghai Institute of Microsystem and Information Technology, Chinese Academy of Sciences, Shanghai 200050, China (e-mail: xguo@mail.sim.ac.cn; jccao@mail.sim.ac.cn; rzhang@mail.sim.ac.cn; zytan@mail.sim.ac.cn).

H. C. Liu is with the Key Laboratory of Artificial Structures and Quantum Control, Department of Physics, Shanghai Jiao Tong University, Shanghai 200240, China (e-mail: h.c.liu@sjtu.edu.cn).

Color versions of one or more of the figures in this paper are available online at <http://ieeexplore.ieee.org>.

Digital Object Identifier 10.1109/JSTQE.2012.2201136

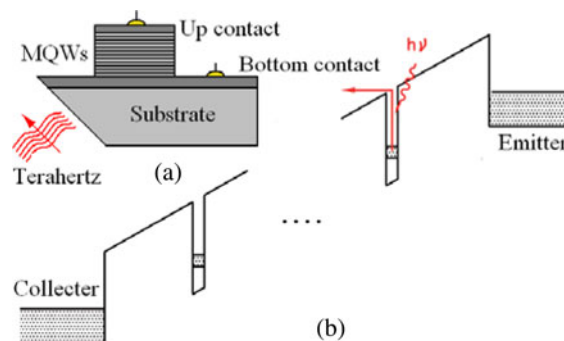


Fig. 1. (a) Device schematic and (b) conduction band profile of an n-type GaAs/(Al,Ga)As 45° facet coupled terahertz QWP.

Combined with the time-delay sampling technique, the photoconductive antennas gated by femto-second laser pulses can detect the magnitude and the phase of a terahertz electric field simultaneously. Schottky barrier diodes can be operated in the temperature range of 4–300 K and used both in direct terahertz detection and as mixers in coherent heterodyne detection systems [7]. Due to the absence of narrow band-gap materials in nature with their interband transition frequencies in terahertz range, there are no terahertz photon detectors based on interband transitions. Two types of terahertz photon detectors have been widely utilized for a long time [8], [9]. The first type is the pair-breaking photon detectors made of low-temperature superconductors, which are sensitive mixers in the low terahertz range [8]. The second-type terahertz photon detectors are fabricated by extrinsic semiconductors based on Ge, Si, GaAs, GaP, etc., in which the electrons bounded by shallow-impurity centers at low temperatures can be excited to conductive bands by terahertz photons [9].

Recently, terahertz quantum-well photodetectors (QWPs) based on intersubband transitions have been realized [10], [11]. Fig. 1 presents a schematic of the typical 45° facet light-coupling geometry and conduction band profile of an n-type GaAs/(Al,Ga)As terahertz QWP. The physical mechanism of photon response of terahertz QWPs is the same as that of QWPs working in the usual thermal infrared region. Under dark condition, because the electrons are bounded to the quantum wells and the direct tunneling between neighboring quantum wells is blocked by the thick barriers, the device is in a high-resistance state. When terahertz radiations are coupled into the terahertz QWP, the bounded electrons in the ground subbands are excited into the first excited subbands and continuum states, a drift photocurrent flows through the biased terahertz QWP, and the device is in a low-resistance state. Consequently, a

TABLE I  
COMPARISON OF MAIN FEATURES OF COMMON TERAHERTZ DETECTORS: NOTE THAT NOISE EQUIVALENT POWER (NEP) IS DETECTOR-AREA DEPENDENT

| Detectors                                   | Operating temperature (K) | NEP (pW/Hz <sup>1/2</sup> ) | Response time (s)                    | Frequency (THz) |
|---|---------------------------|-----------------------------|--------------------------------------|-----------------|
| Golay cell [19]                             | 298                       | 200-400                     | >0.05                                | 0.2-30          |
| VOx bolometers [20]                         | 298                       | ~40                         | >0.01                                | 1.0-10          |
| LiTiO3 pyroelectric detectors [21]          | 298                       | ~400                        | >0.01                                | 0.2-30          |
| Schottky barrier diodes [21]                | 298                       | ~100                        | ~10 <sup>-10</sup>                   | 0.1-10          |
| Superconducting hot-electron bolometers [7] | <4.2                      | 0.1 times the quantum limit | ~2×10 <sup>-10</sup>                 | 0.1-10          |
| Si bolometers [22]                          | 4.2                       | ~0.1                        | >0.025                               | 0.15-20         |
| Pair-breaking detectors [21]                | <<4.2                     | close to quantum limit      | ~2×10 <sup>-10</sup>                 | <2.0            |
| Terahertz QWPs [16]                         | <20.0                     | <10.0                       | <10 <sup>-9</sup> (Not measured yet) | 3.0-7.0         |

For superconducting detectors used as mixers, the ideal quantum limit is  $h\nu$  (photon energy) in unit of W/Hz.

photoconductivity occurs, resulting in the detection of the terahertz radiations. There are two differences between QWPs working in terahertz and mid-infrared. First, due to the small energy difference between the ground and the first excited subbands, many-particle effects are more important in terahertz QWPs. Moreover, since the dark current in QWPs is mainly due to thermal excitation and thermally assisted tunneling of localized electrons in quantum wells, terahertz QWPs must be operated at lower temperatures due to the decrease of barrier height. Second, because of the subwavelength scale of device thickness and a low doping concentration in quantum wells, intersubband absorption efficiency is much lower for terahertz QWPs with standard device geometries, and hence the need for enhancement mechanisms discussed in the paper.

There are several other types of intersubband photodetectors. Photovoltaic terahertz photodetectors based on quantum cascade structures are expected to have low dark current [12]. The terahertz single-photon detector composed by a single-etched quantum-dot (QD) absorber and a single-electron transistor is very sensitive in lower terahertz range (<0.6 THz) at temperatures below 1.0 K [13]. Traditional terahertz QD [14] and quantum-ring (QR) [15] photodetectors were successfully fabricated by using a self-assembled growth method. In comparison with terahertz QWPs, the QD and QR photodetectors have similar performance at low temperatures (<20 K). With increasing temperature, the degradation in performance for QD and QR photodetectors is slower due to the 3-D confinement of electrons.

In comparison with other terahertz detectors, intersubband-transition-based terahertz QWPs display some specific features [16]. Due to the intrinsic short lifetime of photon-excited electrons, terahertz QWPs can be operated with high response speed and therefore suited for high-frequency applications [16], [17]. Terahertz QWPs are narrow-band detectors because of the delta-function-like joint density of states of intersubband transitions.

As a result, filters are not required in some laser-based concealed object imaging applications. The response peak frequency of a terahertz QWP is determined by the energy difference between the first and second subbands of the quantum wells, which can be well designed and implemented with molecular beam epitaxy (MBE) growth technique. The mature semiconductor processing technique makes it possible to fabricate large-scale uniform, high-resolution, and long-term stable focal plane array, which is important for realizing real-time terahertz imaging systems. The main characteristics of common terahertz detectors are listed in Table I. The features of terahertz QWPs mentioned previously make them attractive for potential applications such as terahertz imaging, heterodyne detection, terahertz free space communication, etc.

In this paper, we first discuss the design principle of GaAs/(Al,Ga)As terahertz QWPs. In comparison with the QWPs operating in mid-infrared, because the energy difference between the first and second subbands of terahertz QWPs is much smaller, many-particle effects play an important role in band structures and response peak frequencies of terahertz QWPs. Two main many-particle interactions, the electron exchange-correlation potential, and the depolarization effect are considered within the local density approximation (LDA) [18]. Low intersubband absorption efficiency due to the low electron doping concentration in the quantum wells is a key factor in limiting the performance of terahertz QWPs. In order to improve the intersubband absorption efficiency, three light-coupling schemes, metal diffractive grating couplers, metal-cavity couplers, and surface plasmon polariton (SPP) couplers are investigated. High efficient light couplers are expected to effectively improve the responsivity and working temperature of terahertz QWPs. Finally, the applications of terahertz QWPs in wireless communication and concealed metal object imaging are demonstrated.

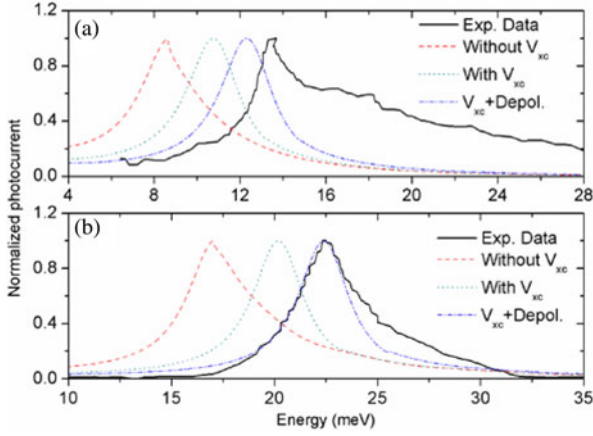


Fig. 2. Calculated and experimental photocurrent spectra of terahertz QWPs: (a) for V267 and (b) for V266.  $V_{xc}$  denotes the exchange–correlation potential.

## II. BAND STRUCTURES AND PHOTOCURRENT SPECTRA OF TERAHERTZ QWPs

We first calculate the band structures and the photocurrent spectra of two devices labeled as V266 and V267 reported in [10] and [11]. The MBE layers consist of a 400-nm top contact layer with Si doping concentration of  $1.0 \times 10^{17}/\text{cm}^3$ ,  $N$  quantum wells with  $L_w$ -wide GaAs layers,  $L_b$ -thick  $\text{Al}_x\text{Ga}_{1-x}\text{As}$  barriers, and an 800-nm bottom contact layer doped with Si to  $1.0 \times 10^{17}/\text{cm}^3$ . The central 10-nm-wide region of each quantum well is doped with Si to  $N_d$ . For V266, the parameters are  $N = 30$ ,  $L_w = 15.5$  nm,  $L_b = 70.2$  nm,  $x = 0.03$ , and  $N_d = 6.0 \times 10^{16}/\text{cm}^3$ . For V267, the parameters are  $N = 23$ ,  $L_w = 22.1$  nm,  $L_b = 95.1$  nm,  $x = 0.015$ , and  $N_d = 3.0 \times 10^{16}/\text{cm}^3$ . The barrier height is  $0.87x$  eV [16]. The electron effective mass is  $0.067m_0$  with  $m_0$  being the free electron mass. The band structures and the photocurrent spectra are determined by the parameters  $L_w$ ,  $x$ , and  $N_d$ . The barrier thickness  $L_b$  is determined by the condition that the direct interwell tunneling is effectively blocked. The absorption efficiency is proportional to the quantum well number  $N$ . Numerical design details are presented in [23].

The effects of the exchange–correlation potential and the depolarization interaction are explored [23]. For V266 and V267, when the electron Coulomb interaction is considered in the Hartree approximation, only one localized subband exists in the quantum well, and the first excited subband is in alignment with the top of the barrier, which is in coincidence with the design rule of bound-to-quasibound QWPs [16]. However, when the exchange–correlation potential is taken into account, the quantum well becomes deeper, which increases the energy difference between the ground subband and the first excited subband and pulls the first excited subband deep into the quantum well. The energy difference between the top of the barrier and the first excited subband  $\Delta E$  is 3.2 meV for V266, and 3.0 meV for V267. The measured photocurrent spectra of the two devices indicate that the photon-excited electrons in the first excited subband can escape into the continuum states via scattering and electric-field-assisted tunneling mechanisms. With further increasing the doping concentration in the quantum well,  $\Delta E$  increases. As a result, instead of escaping, most electrons in the first excited subband are scattered back to the ground subband

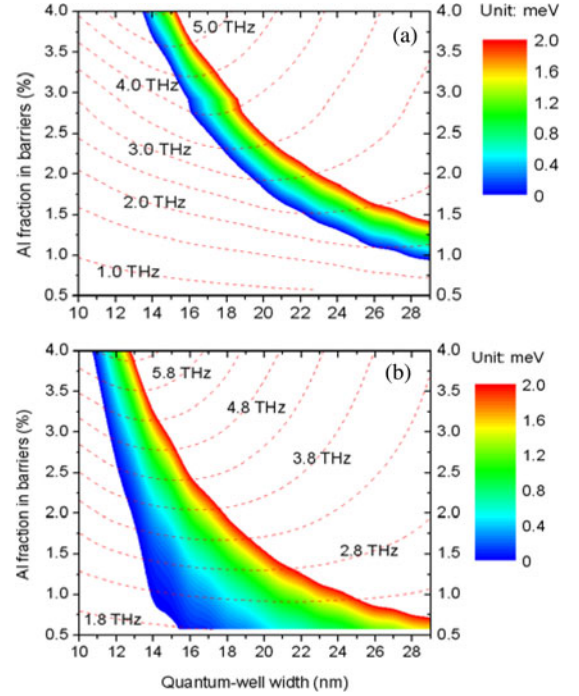


Fig. 3. Calculated well width and barrier Al mole fraction for a GaAs/AlGaAs quantum well (a) without and (b) with the exchange–correlation potential and depolarization considered. The red dotted contour lines present the response peak frequencies; the energy differences between the top of the barrier and the first excited subband are shown by different colors. Si doping concentration in the 10-nm central region of the quantum well is  $4.0 \times 10^{16}/\text{cm}^3$ .

via electron–phonon and other interactions. Therefore, for such heavily doped terahertz QWPs, the localized electrons must be excited to higher subbands, which leads to broadening and blue-shift of the photocurrent peaks [24], [25]. At the same time, the performance is degraded [24].

Theoretical and experimental photocurrent spectra for V266 and V267 are shown in Fig. 2 [23]. In order to obtain physical insights, different many-particle interactions are considered step by step in our calculations. The deviations of response peaks between theory and experiment for V266 and V267 are 5.6 meV (24.8%) and 4.8 meV (36.0%) without including any many-particle interaction. When the exchange–correlation potentials are taken into account, the deviations decrease to 2.4 meV (10.6%) and 2.6 meV (19.4%), respectively. Further improvements of theoretical response peak positions are achieved by considering the depolarization effects, and the discrepancies are about 0.2 meV (0.9%) and 1.1 meV (8.2%) for V266 and V267, respectively. The large remaining discrepancy between theory and experiment for V267 may originate from the fluctuation of Al fraction in barriers due to the small Al mole fraction (1.5%).

The optimal quantum-well parameters for a QWP are to have the first excited subband in alignment with the top of the barrier [16]. If this condition is satisfied, there is a large transition dipole between the ground subband and the first excited subband; and at the same time the photon-excited electrons in the first excited subband can transport to the continuum states effectively. Fig. 3 presents the calculated response peak frequencies (red dotted contour lines) and  $\Delta E$  (color bars,  $0.0 \leq \Delta E \leq 2.0$  meV) in the GaAs/(Al,Ga)As quantum-well parameter space of  $x =$

0.5–4.0% and  $L_w = 10\text{--}30$  nm without and with considering the many-particle interactions. The Si doping concentration is set to  $N_d = 4.0 \times 10^{16}/\text{cm}^3$  in the central 10-nm region of the quantum well. The many-particle interactions significantly affect the band structures and the response peak frequencies, especially for devices working in the lower THz range. For V266 and V267, the energy differences between the top of barrier and the first excited subband are about 2.5 meV [23]. The measured photocurrent spectra of V266 and V267 indicate that the photon-excited electrons in the first excited subbands can transport into the continuum states and contribute to photocurrent. However, if this energy difference increases to about 3.0 meV, the electrons in the first excited subband cannot escape into the continuum states effectively [23], [24]. Therefore, it is expected that most photon-excited electrons in the first excited subband can escape from the quantum well to the continuum states with the value of  $\Delta E$  in the range of 0.0–2.0 meV via scattering and electric-field-assisted tunneling processes. Therefore, it is expected that most photon-excited electrons in the first excited subband can escape from the quantum well to the continuum states with the value of  $\Delta E$  in the range of 0.0–2.0 meV via scattering and electric-field-assisted tunneling mechanisms.

At present, the response frequencies of GaAs/(Al,Ga)As terahertz QWPs cover a frequency range of 3.0–7.5 THz. Terahertz QWPs working for a lower frequency range of 1.0–3.0 THz have not been realized. As shown in Fig. 3(b), for covering 1.0–3.0 THz the Al mole fraction will need to be less than 1.5% for GaAs/(Al,Ga)As terahertz QWPs. It is therefore important to control the accuracy and fluctuation of Al fraction for the growth. Furthermore, because of the decrease of barrier height, low Si concentrations in quantum wells are favored to suppressing the dark current. We are carrying on research in these directions.

### III. LIGHT COUPLERS FOR TERAHERTZ QWPs

Light coupling is another key factor for better performance of terahertz QWPs [16]. Since light absorption in terahertz QWPs is due to intersubband transitions, the selection rule dictates that terahertz QWPs cannot respond to normally incident light. We study three types of metal-grating-based light couplers for terahertz QWPs. For simplicity, only 1-D gratings are considered. All results for the case of 1-D gratings can be easily generalized to the 2-D grating case. The metal grating period is in the  $X$  direction, the length of metal strips is infinite in the  $Y$  direction, and the quantum well growth direction is along the  $Z$ -axis. We define a quantity  $\gamma$ , the normalized coupling efficiency of a light coupler to that of a  $45^\circ$  facet coupling scheme

$$\gamma = \frac{2 \iiint_{\text{MQWs}} |E_z|^2 dv}{\iiint_{\text{MQWs}} |E_0|^2 dv} \quad (1)$$

where  $E_0$  is the electric field intensity in the multiquantum-well (MQW) region of a terahertz QWP with a  $45^\circ$  facet coupling scheme. The factor 2 in (1) accounts for the loss of 50% up-polarized incident photons in the  $45^\circ$  facet coupling geometry. Because of very low mole fraction of Al in the (Al,Ga)As barriers and low Si doping concentration in the quantum wells, we use a homogenous dielectric layer of GaAs to replace the MQW structure, and we also neglect the contribution of intersubband

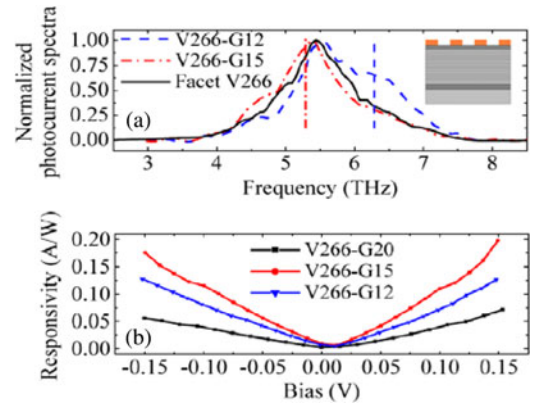


Fig. 4. Normalized photocurrent spectra of V266-G12, V266-G15, and the  $45^\circ$  facet coupled device (Facet V266). The normalized photocurrent spectrum of V266-G20 (not shown) is similar to that of V266-G15. The frequencies marked by the vertical lines are the first-order diffraction mode frequencies of 12- $\mu\text{m}$  grating (blue) and 15- $\mu\text{m}$  grating (red), respectively. (b) Peak responsivities of V266-G12, V266-G15, and V266-G20. The inset to (a) is a schematic of the grating-coupled terahertz QWP.

transitions to the relative permittivity. The approximation makes the designs of light couplers and terahertz QWPs decoupled.

1-D and 2-D diffractive gratings were widely used as light couplers of mid-infrared, far-infrared QWPs [26]–[28]. Three different 1-D metal gratings with periods of  $p = 12.0 \mu\text{m}$  (V266-G12),  $p = 15.0 \mu\text{m}$  (V266-G15), and  $p = 20.0 \mu\text{m}$  (V266-G20) for the device V266 were fabricated and tested [29]. The modal method [30] is employed to analyze the results. The calculated frequencies of the first diffractive modes are 3.80, 5.28, and 6.27 THz for the three gratings, respectively. It is shown that the photocurrent spectrum of V266-G12 is distorted, whereas for V266-G15, the shape remains nearly the same and only shows a small red shift. The vertical lines indicating the positions of the first diffractive modes of the gratings are shown in Fig. 4(a) to explain the distortion. According to our numerical simulations, the incident lights with frequencies indicated by the vertical lines are most efficiently coupled by the following gratings: 5.28 THz for the 15- $\mu\text{m}$ -period grating (red dash-dotted line) and 6.27 THz for the 12- $\mu\text{m}$ -period grating (blue dashed line). Due to this efficient coupling, a shoulder appears around the blue vertical line in the spectrum of V266-G12, and no significant distortion is observed for V266-G15. For the case of V266-G20, the spectrum (not shown) is similar to the  $45^\circ$  facet one. The possible reason is that the spectrum is sharply peaked and, hence, the effect of the grating is not clearly visible. Based on the spectra in Fig. 4(a), peak responsivities of V266 with different gratings are acquired [see Fig. 4(b)]. At 0.15-V bias, the responsivities are 0.128, 0.197, and 0.070 A/W for V266-G12, V266-G15, and V266-G20, respectively, which are much higher than the responsivity of 13 mA/W reported in [31]. Theoretical calculations show that the peak coupling efficiency of an optimized metal grating is about three times larger than that of  $45^\circ$  facet scheme [32]. However, the measured peak responsivity of V266 with  $45^\circ$  facet coupling is about 0.3 A/W at temperature of 8 K and biased voltage of 0.15 V [11], which is larger than that of V266-G15. The possible reason for the discrepancy between theory and experiment may be the extra Joule loss due to the imperfection of metal–semiconductor

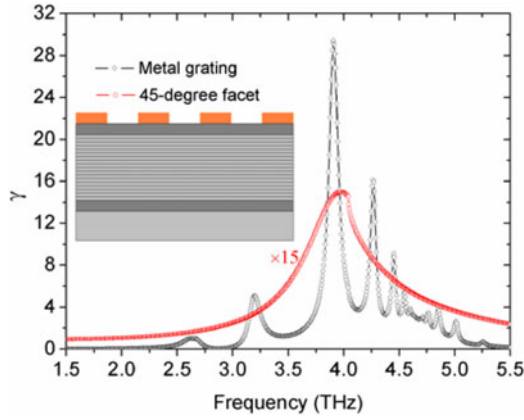


Fig. 5. Calculated photocurrent spectra of metal-grating coupled and 45° facet coupled terahertz QWPs. For clarity, the normalized absorption spectrum of the 45° facet terahertz QWP is multiplied by a factor of 15. The inset shows the device geometry.

interface. Further investigations are needed to address the exact reason of the discrepancy.

SPPs are electromagnetic excitations originating from the collective motion of free electrons, which propagate along the interface between a dielectric and a conductor and are confined in the perpendicular direction [33], [34]. We proposed SPP-based light couplers for terahertz QWPs [35]. Normally, incident light can be coupled into SPP modes supported by the top contact layers of terahertz QWPs by a 1-D metal grating. The resonant coupling peak frequencies are determined by the parameters of metal grating period  $p$ , metal strip width  $s$ , Si doping concentration  $n$  in the top contact layer, and the thickness of the top contact layer  $a$ . Because the thicknesses of the active MQW regions of terahertz QWPs are in subwavelength scale, the evanescent and  $z$ -polarized electric fields related to the SPPs have a large overlap with the MQW regions of terahertz QWPs. Therefore, the SPP-based light couplers are expected to improve the coupling efficiencies of terahertz QWPs significantly. For SPP-based light couplers, the SPP modes are supported by the trilayer air-n-doped GaAs–GaAs structures. In general, for normally incident light, the metal grating provides momentums of  $\pm 2\pi m/p$  with  $m = 1, 2, 3 \dots$  [33]. However, due to the disturbance from the metal strips on the trilayer structure, we found that the momentums provided by the metal grating are  $\pm 2\pi m/(p - s)$  [35]. The modes characterized by  $\pm m$  correspond to two counterpropagating plane waves having the same frequency. In the phase-matched condition of  $p = m\lambda$  with  $\lambda$  the wavelength, the two counterpropagating plane waves form standing wave patterns. When the values of the device parameters  $p$ ,  $s$ ,  $n$ , and  $a$  are given, aided by the SPP dispersion relation for the trilayer structure [34], resonant coupling frequencies are determined. The electric-field distributions are numerically calculated using an electromagnetic simulation software package based on the finite element method (FEM) [36]. Fig. 5 presents the calculated normalized photocurrent spectra for the 45° coupling scheme and the SPP-based light coupler. The grating parameters are  $p = 16.0 \mu\text{m}$  and  $s = 8.0 \mu\text{m}$ . The metal strips are  $0.5 \mu\text{m}$  thick. The Si doping concentration is  $5.0 \times 10^{17}/\text{cm}^3$  in the  $0.4\text{-}\mu\text{m}$ -thick top contact layer. The Al mole fraction is 2.2% in the (Al,Ga)As barriers. The width of the GaAs quantum wells

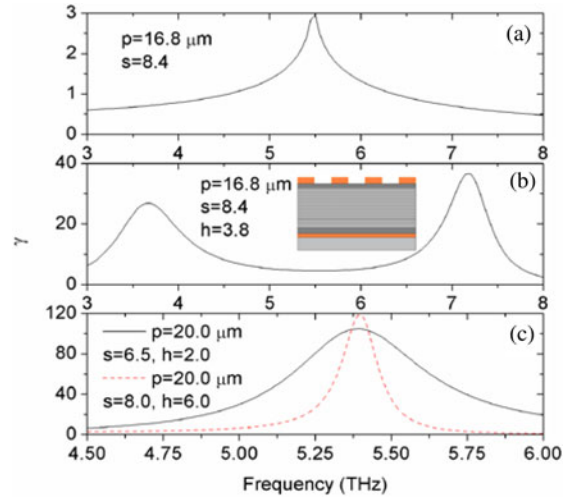


Fig. 6. Numerical results of normalized coupling efficiencies of metal-grating couplers and metal-cavity couplers for terahertz QWPs. (a) Metal-grating coupler. (b) Metal-cavity coupler with the same grating parameters shown in (a). (c) Optimal metal-cavity couplers for terahertz QWPs with the response peak frequency of 5.48 THz. The inset to (b) is a schematic of the cavity-coupled terahertz QWP.

is 15.0 nm, and the Si doping concentration in the central 10-nm-wide regions of the quantum wells is  $4.0 \times 10^{16}/\text{cm}^3$ . The resonant coupling peaks shown in Fig. 5 correspond to different values of  $m$ . The response peak of the terahertz QWP is designed to match the second resonant coupling peak at 3.91 THz. There is a large overlap between the response peak of the QWP and the resonant coupling peaks induced by the SPPs. A maximum value of about 30-fold enhancement of the coupling efficiency is achieved in comparison with that of the 45° facet coupling scheme.

Recently, strong interactions of a localized light field and intersubband transitions in MQWs sandwiched between a metal grating and a bottom metal layer have been systematically investigated [37], [38]. In such subwavelength metal cavity structures, the normally incident light coming from the grating side is strongly compressed into the metal cavity at some resonant frequencies determined by the geometry and material parameters of the grating-MQWs-metal composite structures, and the polarization of the field is effectively tuned to fulfill the intersubband transition selection rule. In a metal-cavity coupled terahertz QWP, a thin metal layer is inserted beneath the bottom contact layer. A subwavelength cavity having high confinement factor is formed between the metal grating and the bottom thin metal layer. We found that the resonant coupling behaviors of a metal cavity are very different from those of a metal grating (see Fig. 6) [32]. The relative dielectric constant and the conductivity of gold, and the relative dielectric constant of GaAs are set to  $-1.80 \times 10^4$ ,  $4.56 \times 10^7 \text{ S/m}$ , and 10.6, respectively in our calculations. The FEM numerical resonant coupling peak of the metal grating is at 5.48 THz [see Fig. 6(a)], which is in accordance with the analytical solution of the first-order diffractive mode frequency  $\nu = c/\sqrt{\epsilon p}$ , where  $c$  is the light speed in vacuum. However, in the metal-cavity coupled terahertz QWPs, the original grating-determined resonant coupling peak at 5.48 THz disappears, and two other resonant

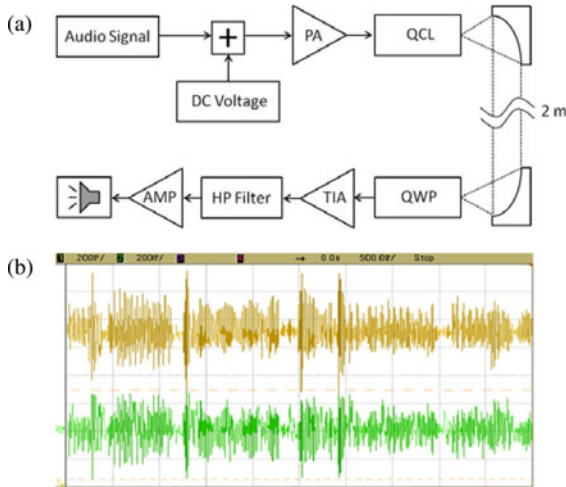


Fig. 7. Wireless audio signals transmission system based on a terahertz QCL and a terahertz QWP. (a) Scheme of the terahertz transmission setup. (b) Time traces of audio signals transmitted over the link, upper trace: modulator signal and lower trace: received signal.

coupling peaks with their maximum values at 3.65 and 7.20 THz emerge with the same grating parameters and the thickness of the cavity  $h = 3.8 \mu\text{m}$  [see Fig. 6(b)]. In comparison with the case of metal-grating-coupled terahertz QWPs, the maximum coupling efficiency increases by about an order of magnitude. The waveguide effects of the metal cavity are responsible for the changes of the resonant coupling behaviors. A ray propagation method [39], [40] is successfully used to analyze the resonant behaviors in the metal-cavity-coupled terahertz QWPs qualitatively. The theoretical maximum value of normalized coupling efficiency  $\gamma$  is about 100 for the optimal metal cavity parameters [see Fig. 6(c)].

For the metal-cavity- and SPP-based light couplers for terahertz QWPs, at resonant coupling frequencies, the polarization of light field is effectively changed to fulfill the intersubband transition selection rule. Meanwhile, the electric field intensity in the active MQW regions of terahertz QWPs is substantially enhanced, which indicates that a higher absorption efficiency is expected for a low Si doping concentration in the quantum wells. The tradeoff [16] between the responsivity and the operating temperature determined by the Si doping concentration in the quantum wells needs to be re-evaluated.

#### IV. APPLICATIONS OF TERAHERTZ QWPs

Due to the intrinsic short lifetime of photon-excited electrons [16], [17], terahertz QWPs are potentially suited for applications in high-speed terahertz communications. We demonstrated an audio terahertz wireless transmission link [41]. A terahertz quantum cascade laser (QCL) [42] is used as the signal emitter and a terahertz QWP as the receiver. The experimental setup is shown in Fig. 7(a). The lasing frequency of the QCL is 4.1 THz. The audio signal from a MP3 player is added to a dc current offset, and amplified by a power amplifier (PA). The modulated bias voltage from the PA is used to driven the QCL. The light amplitude from the QCL operated in linear bias range is proportional to the drive bias voltage. The modulated laser beam is collimated by an off-axis parabolic

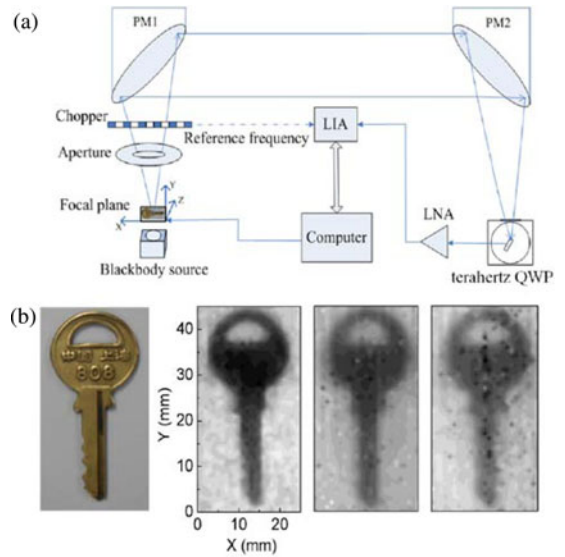


Fig. 8. Scanning terahertz imaging of a concealed metal key with a blackbody source and a terahertz QWP. (a) Schematic of the terahertz imaging setup. (b) Comparison of the concealed metal key between optical picture (left) and terahertz images with different blackbody temperatures of 473, 423, and 373 K (from left to right).

mirror. After a transmission distance of about 2.0 m, the laser beam is focused onto the QWP. The photocurrent is amplified by a transimpedance amplifier (TIA). A high-pass filter is used to eliminate low-frequency noises. The 3-dB bandwidth of the wireless link is about 580 kHz. The oscilloscope traces of the modulated signal and the received signal are shown in Fig. 7(b). The main signal features are well kept, and the audio signal is reproduced via a loudspeaker on the receiving side.

By utilizing the narrow-band response feature of terahertz QWPs, we presented a 2-D-scan terahertz imaging of a metal key in an envelope assisted by a blackbody source [43]. A terahertz QWP with a response peak frequency of 3.2 THz [10] is placed on the 3.4 K cold finger of a close-cycle optical cryostat with a high-density polyethylene window. The experiment setup is shown in Fig. 8(a). The sample is placed at the focal plane of an off-axis parabolic mirror (PM1) and mounted on a computer controlled X-Y translation stage. In front of the sample, we use a pinhole to reduce the background noise. After a chopper, the transmission signal is collimated by PM1 and focused by PM2 onto the terahertz QWP. The photocurrent is amplified by a low-noise amplifier (LNA), and then read out by a lock-in amplifier (LIA) which is controlled by a computer for synchronization with the X-Y stage. Fig. 8(b) presents three images of the concealed metal key with different blackbody temperatures of 473, 423, and 373 K. The corresponding signal-to-noise ratios are 27, 17, and 10, respectively. As the signal-to-noise ratio increases, the quality of the image becomes better. The spatial resolution of the imaging system is  $\sim 1$  mm, which is limited by the scanning system.

#### V. CONCLUSION

In conclusion, intersubband-transition-based terahertz QWPs have some specific features such as intrinsic high response speed, narrow band response, and mature fabrication technique.

They have potential applications such as terahertz imaging, heterodyne detection, terahertz free space communication, etc. Due to the small barrier height and the energy difference between the ground subband and the first excited subband, many particle interactions play key roles in the band structure and the response peak frequency of a terahertz QWP. Because the exchange–correlation potential is negative, it increases the energy difference between the top of the barrier and the first excited subband  $\Delta E$ . A blue shift of the response peak is introduced by both the exchange–correlation and depolarization interactions. Light coupling is another key factor for better performance of terahertz QWPs. Three types of light couplers are investigated. For the metal-cavity- and SPP-based light couplers, at resonant coupling frequencies, the polarization of light field is effectively changed. Meanwhile, the electric field intensity in the active MQW regions of terahertz QWPs is substantially enhanced. Terahertz-QWP-based wireless communication and imaging are demonstrated, which indicates that the terahertz QWPs have potential applications in the aforementioned fields.

#### ACKNOWLEDGMENT

The authors would like to thank their colleagues and coworkers for their contributions, especially Z. Chen and T. Zhou at Shanghai Institute of Microsystem and Information Technology.

#### REFERENCES

- [1] B. Ferguson and X.-C. Zhang, "Materials for terahertz science and technology," *Nat. Mater.*, vol. 1, pp. 26–33, Jan. 2002.
- [2] S. Hargreaves and R. A. Lewis, "Terahertz imaging: Materials and methods," *J. Mater. Sci.: Mater. Electron.*, vol. 18, pp. S299–S303, Mar. 2007.
- [3] J. Wei, D. Olaya, B. S. Karasik, S. V. Pereverzev, A. V. Sergeev, and M. E. Gershenson, "Ultrasensitive hot-electron nanobolometers for terahertz astrophysics," *Nat. Nanotechnol.*, vol. 3, pp. 496–500, Jul. 2008.
- [4] M. Tarasov and L. Kuz'min, "Concept of a mixer based on a cold-electron bolometer," *JETP Lett.*, vol. 81, pp. 538–541, Apr. 2005.
- [5] A. Dobroiu, M. Yamashita, Y. N. Ohshima, Y. Morita, C. Otani, and K. Rawase, "Terahertz imaging system based on a backward-wave oscillator," *Appl. Opt.*, vol. 43, pp. 5637–5646, Oct. 2004.
- [6] M. Tani, K.-S. Lee, and X.-C. Zhang, "Detection of terahertz radiation with low-temperature-grown GaAs-based photoconductive antenna using 1.55  $\mu\text{m}$  probe," *Appl. Phys. Lett.*, vol. 77, pp. 1396–1398, Jun. 2000.
- [7] H.-W. Hubers, "Terahertz heterodyne receivers," *IEEE J. Sel. Topics Quantum Electron.*, vol. 14, no. 2, pp. 378–391, Apr. 2008.
- [8] G. H. Rieke, *Detection of Light: From the Ultraviolet to the Submillimeter*. Cambridge: Cambridge Univ. Press, 2003.
- [9] E. Burstein, J. J. Oberly, and J. W. Davisson, "Infrared photoconductivity due to neutral impurities in silicon," *Phys. Rev.*, vol. 89, pp. 331–332, Jan. 1953.
- [10] H. C. Liu, C. Y. Song, A. J. SpringThorpe, and J. C. Cao, "Terahertz quantum-well photodetector," *Appl. Phys. Lett.*, vol. 84, pp. 4068–4070, May 2004.
- [11] H. Luo, H. C. Liu, C. Y. Song, and Z. R. Wasilewski, "Background-limited terahertz quantum-well photodetector," *Appl. Phys. Lett.*, vol. 86, pp. 231103-1–231103-3, Jun. 2005.
- [12] M. Graf, G. Scalari, D. Hofstetter, J. Faist, H. Beere, E. Linfield, D. Ritchie, and G. Davies, "Terahertz range quantum well infrared photodetector," *Appl. Phys. Lett.*, vol. 84, pp. 475–477, Nov. 2003.
- [13] S. Komiyama, "Single-photon detectors in the terahertz range," *IEEE J. Sel. Topics Quantum Electron.*, vol. 17, no. 1, pp. 54–66, Jan./Feb. 2011.
- [14] X. H. Su, J. Yang, P. Bhattacharya, G. Ariyawansa, and A. G. U. Perera, "Terahertz detection with tunneling quantum dot intersublevel photodetector," *Appl. Phys. Lett.*, vol. 89, pp. 031117-1–031117-3, Jul. 2006.
- [15] G. Huang, W. Guo, P. Bhattacharya, G. Ariyawansa, and A. G. U. Perera, "A quantum ring terahertz detector with resonant tunnel barriers," *Appl. Phys. Lett.*, vol. 94, pp. 101115-1–101115-3, Mar. 2009.
- [16] H. Schneider and H. C. Liu, *Quantum Well Infrared Photodetectors: Physics and Applications*. Berlin: Springer, 2007.
- [17] R. Paiella, F. Capasso, C. Gmachl, D. L. Sivco, J. N. Baillargeon, A. L. Hutchinson, A. Y. Cho, and H. C. Liu, "Self-mode-locking of semiconductor lasers with giant ultrafast optical nonlinearities," *Science*, vol. 290, pp. 1739–1742, Dec. 2000.
- [18] W. Kohn and L. J. Sham, "Self-consistent equations including exchange and correlation effects," *Phys. Rev.*, vol. 140, pp. A1133–A1138, Nov. 1965.
- [19] F. F. Sizov, V. P. Reva, A. G. Golenkov, and V. V. Zabudsky, "Uncooled detector challenges for THz/sub-THz arrays imaging," *J. Infrared Millim. Terahertz Waves*, vol. 32, pp. 1192–1206, Apr. 2011.
- [20] N. Oda, "Uncooled bolometer-type terahertz focal plane array and camera for real-time imaging," *C. R. Phys.*, vol. 11, pp. 496–509, Aug. 2010.
- [21] A. Rogalski and F. Sizov, "Terahertz detectors and focal plane arrays," *Opto-Electron. Rev.*, vol. 19, pp. 346–404, Sep. 2011.
- [22] [Online]. Available: <http://www.infraredlaboratories.com/>
- [23] X. G. Guo, Z. Y. Tan, J. C. Cao, and H. C. Liu, "Many-body effects on terahertz quantum well detectors," *Appl. Phys. Lett.*, vol. 94, pp. 201101-1–201101-3, Apr. 2009.
- [24] M. Graf, E. Dupont, H. Luo, S. Haffouz, Z. R. Wasilewski, A. J. SpringThorpe, D. Ban, and H. C. Liu, "Terahertz quantum well infrared detectors," *Infrared Phys. Technol.*, vol. 52, pp. 289–293, Jun. 2009.
- [25] X. G. Guo, R. Zhang, H. C. Liu, A. J. SpringThorpe, and J. C. Cao, "Photocurrent spectra of heavily doped terahertz quantum well photodetectors," *Appl. Phys. Lett.*, vol. 97, pp. 021114-1–021114-3, Jul. 2010.
- [26] K. W. Goossen and S. A. Lyon, "Grating enhanced quantum well detector," *Appl. Phys. Lett.*, vol. 47, pp. 1257–1259, Sep. 1985.
- [27] J. Y. Andersson and L. Lundqvist, "Near-unity quantum efficiency of AlGaAs/GaAs quantum well infrared detectors using a waveguide with a doubly periodic grating coupler," *Appl. Phys. Lett.*, vol. 59, pp. 857–859, Aug. 1991.
- [28] J. Y. Andersson and L. Lundqvist, "Grating-coupled quantum-well infrared detectors: Theory and performance," *J. Appl. Phys.*, vol. 71, pp. 3600–3610, Apr. 1992.
- [29] R. Zhang, X. G. Guo, C. Y. Song, M. Buchanan, Z. R. Wasilewski, J. C. Cao, and H. C. Liu, "Metal grating coupled terahertz quantum well photodetectors," *IEEE Electron Device Lett.*, vol. 32, no. 5, pp. 659–661, May 2011.
- [30] Y. Todorov and C. Minot, "Modal method for conical diffraction on a rectangular slit metallic grating in a multilayer structure," *J. Opt. Soc. Amer. A, Opt. Image Sci.*, vol. 24, pp. 3100–3114, Oct. 2007.
- [31] M. Patrashin and I. Hosako, "Terahertz frontside-illuminated quantum well photodetector," *Opt. Lett.*, vol. 33, pp. 168–170, Jan. 2008.
- [32] X. G. Guo, R. Zhang, J. C. Cao, and H. C. Liu, "Numerical study on metal cavity couplers for terahertz quantum well photodetectors," *IEEE J. Quantum Electron.*, vol. 48, no. 5, pp. 728–733, May 2012.
- [33] H. Raether, *Surface Plasmons*. Berlin: Springer, 1988.
- [34] S. A. Maier, *Plasmonics: Fundamentals and Applications*. Berlin: Springer, 2007.
- [35] X. G. Guo, R. Zhang, J. C. Cao, and H. C. Liu, "Surface plasmon enhanced absorption in metal grating coupled terahertz quantum well photodetectors," unpublished.
- [36] COMSOL, Multiphysics modeling and simulation software. [Online]. Available: [www.comsol.com](http://www.comsol.com)
- [37] Y. Todorov, A. M. Andrews, I. Sagnes, R. Colombelli, P. Klang, G. Strasser, and C. Sirtori, "Strong light-matter coupling in subwavelength metal-dielectric microcavities at terahertz frequencies," *Phys. Rev. Lett.*, vol. 102, pp. 186402-1–186402-4, May 2009.
- [38] Y. Todorov, L. Tusetto, J. Teissier, A. M. Andrews, P. Klang, R. Colombelli, I. Sagnes, G. Strasser, and C. Sirtori, "Optical properties of metal-dielectric-metal microcavities in the THz frequency range," *Opt. Express*, vol. 18, pp. 13886–13907, Jun. 2010.
- [39] D. Rosenblatt, A. Sharon, and A. A. Friesem, "Resonant grating waveguides structure," *IEEE J. Quantum Electron.*, vol. 33, no. 11, pp. 2038–2059, Nov. 1997.
- [40] A. Sharon, S. Glasberg, D. Rosenblatt, and A. A. Friesem, "Metal-based resonant grating waveguide structures," *J. Opt. Soc. Amer. A*, vol. 14, pp. 588–595, Mar. 1997.
- [41] Z. Chen, Z. Y. Tan, Y. J. Han, R. Zhang, X. G. Guo, H. Li, J. C. Cao, and H. C. Liu, "Wireless communication demonstration at 4.1 THz using quantum cascade laser and quantum well photodetector," *Electron Lett.*, vol. 47, no. 17, Aug. 2011.
- [42] H. Luo, S. R. Laframboise, Z. R. Wasilewski, G. C. Aers, H. C. Liu, and J. C. Cao, "Terahertz quantum-cascade lasers based on a three-well active module," *Appl. Phys. Lett.*, vol. 90, pp. 041112-1–041112-3, Jan. 2007.
- [43] T. Zhou, R. Zhang, X. G. Guo, Z. Y. Tan, Z. Chen, J. C. Cao, and H. C. Liu, "Terahertz imaging with quantum well photodetectors," unpublished.



**X. G. Guo** was born in Liaoning, China. He received the Bachelor's and Master's degrees in physical electronics from Fudan University, Shanghai, China, in 1997 and 2000, respectively, and the Ph.D. degree in microelectronics and solid-state electronics from the Shanghai Institute of Technical Physics, Chinese Academy of Sciences, Shanghai, in 2003.

He is currently an Associate Professor of the Key Laboratory of Terahertz Solid-State Technology, Shanghai Institute of Microsystem and Information Technology, Chinese Academy of Sciences. His major research interest includes terahertz semiconductor optoelectronic devices.

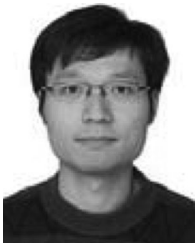


**J. C. Cao** was born in Jiangxi, China, in 1967. He received the Ph.D. degree in electrical engineering from the Southeast University, Nanjing, China, in 1994.

He is currently the Terahertz (THz) group leader and Director of the Key Laboratory of Terahertz Solid-State Technology, Shanghai Institute of Microsystem and Information Technology, Chinese Academy of Sciences, Shanghai, China. From 1999 to 2000, he was a Senior Visiting Scientist at the National Research Council, Ottawa, Canada. He and

his group members successfully developed THz quantum cascade laser and its applications in THz communication and imaging, developed Monte Carlo simulation method for THz quantum cascade lasers, developed THz-radiation-induced semiconductor impact ionized model, and successfully explained the absorption of strong THz irradiation in a low-dimensional semiconductor. His current research interests include THz semiconductor devices and their applications.

Dr. Cao received the National Fund for Distinguished Young Scholars of China and the Natural Science Award of Shanghai (the Peony Award) in 2004. He got the Excellent Teacher Award from Chinese Academy of Sciences twice in 2006 and in 2011.



**R. Zhang** was born in Nanjing, China. He received the Bachelor's degree in biological physics from Nanjing University, Nanjing, and the Doctor's degree in microelectronics and solid-state electronics from the Shanghai Institute of Microsystem and Information Technology (SIMIT), Chinese Academy of Sciences, Shanghai, China, in 2006 and 2011, respectively.

He is currently an Assistant Research Fellow of SIMIT. His major research interests include terahertz semiconductor devices and their applications.



**Z. Y. Tan** was born in Hunan, China, in 1982. He received the Bachelor's degree in electronic science and technology from Jilin University, Jilin, China, and the Ph.D. degree in microelectronics and solid-state electronics from the Shanghai Institute of Microsystem and Information Technology (SIMIT), Chinese Academy of Sciences, Shanghai, China in 2005 and 2010, respectively.

He is currently an Assistant Research Fellow of SIMIT. His activities are mainly concerned with terahertz semiconductor devices and their applications, particularly for the generation, transmission, and detection of terahertz light.



**H. C. Liu** (M'99–SM'05–F'07) was born in Taiyuan, China. He received the B.Sc. degree in physics from Lanzhou University, Lanzhou, China, in 1982, went to the U.S. in the same year via the CUSPEA program, and received the Ph.D. degree in applied physics from the University of Pittsburgh, Titusville, in 1987 as an Andrew Mellon Predoctoral Fellow.

He was with the Institute for Microstructural Sciences of the National Research Council of Canada from 1987 to 2011. He is currently with the Shanghai Jiao Tong University, Shanghai, China, as a "1000"

Chair Professor. He has published extensively in refereed journals with an H-index of 38 and presented often in international conferences with about 90 plenary/invited talks. His major research interest includes semiconductor quantum devices.

Dr. Liu has been elected as a Fellow of the Academy of Sciences—Royal Society of Canada and a Fellow of the American Physical Society. He received the Herzberg Medal from the Canadian Association of Physicists in 2000, the Bessel Prize from the Alexander von Humboldt Foundation in 2001, the Distinguished Young Scientist Award (NSFC-B) in 2005, and the Changjiang Scholar Award in 2008.